Modeling and Control of WPT Systems in the Presence of Load and Mutual Inductance Variations

Shijun Zhao, *Member, IEEE*, Fengwei Chen, Chunsen Tang, *Member, IEEE*, Pengqi Deng, *Student Member, IEEE*, and Chanzhen Duan, *Student Member, IEEE*

***Abstract*—The low-order Hammerstein model plus time delay has been a popular option to describe the dynamic behavior of a wireless power transfer (WPT) system. The controller designed based on this model can achieve better set point tracking performance in a computationally efficient way. Furthermore, load and mutual inductance variations are quite common in WPT systems and they will impair the modeling accuracy and control performance if one has not been taken into account. To address this problem, this article proposes a combined internal model control (IMC) and Luenberger disturbance observer (LDO) method to achieve enhanced disturbance rejection performance against load and mutual inductance variations. Specifically, a data-driven method is employed to build the system model, then the IMC-based method is proposed for controller design, in which LDO is combined to observe and eliminate the disturbances. To ensure the stability of the closed-loop system, a pole placement method is suggested to properly design the observer gain. Thanks to the LDO that can accurately estimate the disturbances resulting from load and mutual inductance variations, the IMC controller can rapidly track the set point irrespective the disturbances. Finally, simulation and experimental results are provided to validate the effectiveness of the proposed method.**

***Index Terms*—Data-driven modeling, disturbance rejection control, internal model control (IMC), Luenberger disturbance observer (LDO), wireless power transfer (WPT).**

I. Introduction

WIRELESS power transfer (WPT) based on magnetic resonant coupling has many advantages, such as less physical contact, significant reliability, and flexibility [1], [2], [3], so it has been practiced widely in various fields, especially in the portable devices, biomedical engineering, electric vehicles, marine industries, oil drilling [4], [5], [6], [7], [8]. In practical operation, uncertainties exist in the load of WPT systems, and gaps between primary and secondary coupling mechanisms can lead to fluctuations in system mutual inductance parameters. In addition, environmental factors may induce variations in circuit parameters. Due to these factors, system outputs inevitably exhibit instability, potentially leading to electrical equipment damage. To address the output instability resulting from changes or fluctuations in mutual inductance or load parameters, numerous researchers have conducted extensive investigations. Particular coil structure designs can be used to suppress fluctuations in mutual inductance [9], [10], [11], [12]. Resonant network topology design can impart a quasi-constant current/voltage characteristic to the system's output, effectively mitigate fluctuations caused by load variations [13], [14], [15]. Both methods are relatively simple to implement. However, specific coil structures can only effectively suppress output fluctuations caused by mutual inductance disturbances in some systems, and suppressing load disturbances is ineffective. A specific topology design can only effectively suppress output fluctuations caused by load disturbances, and suppressing mutual inductance disturbances is ineffective. Therefore, closed-loop control methods are necessary to achieve more accurate and stable system outputs. Typically, closed-loop control encompasses secondary-side and primary-side control.

Currently, secondary-side control methods mainly involve adding additional dc–dc converters to suppress output fluctuations. Liu et al. [16] proposed a PI passivity-based control (PIPBC) method to ensure stable system output in the presence of mutual inductance disturbances. In [17], a discrete-sliding-mode control (DSMC) was devised to achieve constant output voltage. Zhou et al. [18] proposed a model predictive control (MPC) strategy to ensure system output stability by adjusting the output voltage. Wang et al. [19] introduced a hybrid control strategy to mitigate system output fluctuations. Zhang et al. [20] proposed an output regulation and disturbance observer (ORDOB) method to maintain constant output voltage by adjusting the duty cycle of the dc converter. This approach effectively suppresses output voltage fluctuations in the presence of mutual inductance variations. These methods have the following characteristics. The output is directly sampled on the secondary side for feedback control, avoiding the need for communication links. Those components added in the dc–dc converter, including switching devices, large capacitors, and inductors, will increase system size, reduce overall efficiency under nominal operating conditions, and increase the system's dynamic response time. Note that in such secondary dc–dc controlled WPT systems, the wireless link is simplified as a dc voltage source (i.e., the

Manuscript received 15 February 2024; revised 2 May 2024 and 23 June 2024; accepted 17 July 2024. Date of publication 23 July 2024; date of current version 11 September 2024. This work was supported by the National Natural Science Foundation of China under Grant 52277002 and Grant 62073246. Recommended for publication by Associate Editor M. Ponce-Silva. *(Corresponding author: Fengwei Chen.)*

Shijun Zhao, Fengwei Chen, Chunsen Tang, and Chanzhen Duan are with the School of Automation, Chongqing University, Chongqing 400044, China (e-mail: zsjwpt@cqu.edu.cn; fengwei.chen@cqu.edu.cn; cstang@cqu.edu.cn; duancz@stu.cqu.edu.cn).

Pengqi Deng is with the College of Optoelectronics Engineering, Chongqing University of Posts and Telecommunications, Chongqing 400065, China (e-mail: dengpq@cqupt.edu.cn).

Color versions of one or more figures in this article are available at https://doi.org/10.1109/TPEL.2024.3432571.

Digital Object Identifier 10.1109/TPEL.2024.3432571

dynamics of the wireless link is neglected), so in the modeling and control of the system is the same than that of a conventional dc–dc converter.

Primary-side control includes indirect closed-loop control and direct closed-loop control as follows.

1) The indirect control methods based on primary-side parameters identification can estimate appropriate the phase-shifting (PS) angle to ensure output stability. This method involves real-time sampling of the output current and the output voltage of the inverter in primary side to identify mutual inductance or load parameters. The entire process is completed solely at the primary side [21], [22], [23], without the wireless communication. Typically, this method necessitates prior knowledge of certain system parameters, such as mutual inductance or load. Usually, this method requires that the unidentified parameters of the system are known, and that the system parameters and topology remain unchanged. The complex identification algorithms may result in significant output control delays. In practical operation, system parameters may deviate or be unknown, leading to identification challenges. This method lacks real-time feedback on the system output, which may lead to delayed output adjustment, reduced adjustment accuracy, and thus, affect the stability of the system.
2) The combination of primary-side dc–dc converter and communication can achieve direct closed-loop control. The research in this area mainly focuses on improving the efficiency of the system [24], [25], [26]. The systems that apply such methods have low efficiency and large volume. In addition, the combination of communication feedback and primary-side PS control can also achieve direct closed-loop feedback control of system output. This approach offers the benefits of simplicity, lightweight design, and easy implementation, facilitating precise control of the secondary output. The related research mainly focuses on establishing dynamic models of the system [27], [28]. The case of the time-varying parameter perturbations is not considered in the design of the controller, which may cause instability in the output.

Therefore, the method of combining communication feedback with primary-side PS control for output adjustment is adopted in this article. Nonlinear issues can arise due to the switching devices of the inverter in PS control process. In actual operation, changes or disturbances in the parameters of the WPT system may occur due to environmental and aging reasons, posing challenges in the design of the control system. Therefore, it is necessary to establish the system model and adopt appropriate control methods to ensure the stability of the system. Traditional modeling methods for the WPT system include generalized state-space averaging [29], ac impedance analysis [30], etc., have the disadvantage of relying on specific system parameters, while data-driven modeling infers the system model parameters and communication delays through input–output data [31], which is more suitable for control system design. The Hammerstein model, which consists of a static input nonlinearity function followed by a linear transfer model, is an effective model to describe the dynamic behavior of a primary side PS controlled WPT system [27], [28], [32], [33]. Furthermore, if the load and mutual inductance is time varying, the linear parameter-varying (LPV) Hammerstein model could be a more accurate choice [34]. However, in this article, the LPV Hammerstein model will not be considered. We adopt the simpler Hammerstein model plus disturbance structure, where the Hammerstein model is used to capture the dominant behavior of the system while the disturbance is used to describe uncertainties resulting from the coupling or load variations.

Usually, in closed-loop systems, the controller and observer are used simultaneously to achieve precise output control and state estimation [35]. This combination can provide the advantage of two-degree of freedom, not only achieving precise reference tracking, but also significantly enhancing the disturbance suppression ability of the closed-loop system. The internal model control (IMC) has the advantages of low-computational burden and simple implementation [36]. In our previous work [27], a voltage controller was designed based on the IMC principle considering pure communication delay compensation. This not only reduce adjustable parameters, but also improves the robustness of the system. However, there are two issues that have not been considered as follows: First, the parameters of the controller for the tracking performance and the disturbance rejection performance need to be separated. Second, the IMC remains unchanged under time-varying disturbances, which may not guarantee the stability of the system. In other words, the IMC may not effectively eliminate disturbances caused by model mismatches [37]. Currently, the most commonly used observers for system state estimation and disturbance compensation include disturbance observer (DOB), extended state observer (ESO), and Luenberger disturbance observer (LDO). The DOB is designed using the inverse of the system model and requires an addition of extra filters [20], [38]. Due to limitations in filter design, in some cases, it will affect the dynamic performance of the system [38]. The traditional ESO is generally used in the design of active disturbance rejection control systems [39], [40]. It does not rely on the accurate system model, requiring only knowledge of the system's order and approximate dynamic characteristics. The application of the ESO in systems with the time-delay link is relatively less explored. The LDO can estimate unknown state variables, which has the advantages of being simple and easy to implement, exhibiting relative robustness to system parameter variations and measurement noise [41], [42]. It performs exceptionally well in the real-time estimation of linear system states online. In the field of power electronics, the LDO has been gradually studied due to its superiority [43], [44], [45]. Both LDO and IMC methods are designed based on the linear model, making it convenient to combine IMC method with LDO. To enhance control performance in the presence of disturbances, we introduce the LDO into the WPT system to compensate for time-varying disturbances in real-time through a feedforward loop. Based on the Hammerstein-model-based IMC method proposed in our previous research [27], in this article, we proposed an IMC-LDO method to more effectively handle disturbances caused by load and mutual inductance variations. In the first step, we identify a

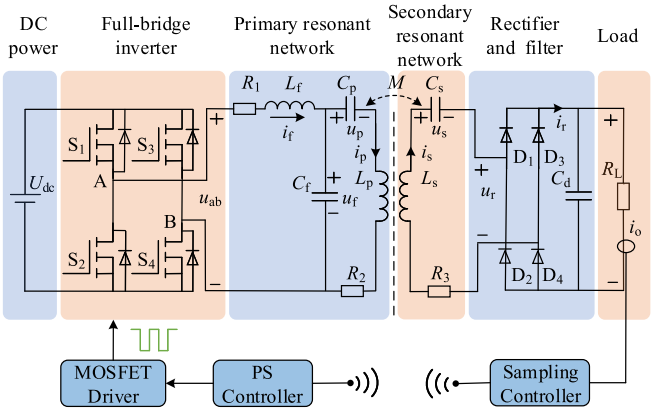

Fig. 1. Example of the PS control for load current.

Hammerstein model with time delay for the WPT system from experimental data. Then, based on the identified model, the LDO is constructed and combined with the IMC to enhance the quality of load current control under time delay and a varying mutual inductance. Especially, the nonlinearity and time delay of the system need to be taken into account for observer design. For the LDO, the tracking performance of state estimation is determined by the observer poles, so a pole placement algorithm is also introduced to adjust the observer gain. The two main features of the proposed IMC-LDO scheme for the WPT system are listed as follows:

1) A controller based on IMC-LDO structure is proposed to address the issue of output fluctuations caused by changes in parameters, such as mutual inductance and load in the system, in order to accurately and quickly compensate for disturbances and ensure the stability of the system's output.
2) An LDO structure considering nonlinearity and time delay is proposed, and parameters are designed using pole placement method. The fast and accurate estimation of overall disturbances in the WPT system is achieved.

The rest of this article is organized as follows. In Section II, a Hammerstein model for the *LCC-S* WPT system that relates the duty cycle and load current is established, and an IMC controller is designed. In Section III, the LDO design is introduced and the combination method of the conventional IMC and LDO is illustrated. Subsequently, in Sections IV and IV, the simulation and experimental results are presented to demonstrate the validity of the IMC-LDO. Finally, Section VI concludes this article.

II. System Modeling and IMC Method

A. System Description and Dynamic Modeling

In this article, the *LCC-S* WPT system with second-order output characteristics is studied as a typical example. Fig. 1 illustrates a typical closed-loop control structure for the *LCC-S* WPT system.

The primary side comprises a dc power supply, a full-bridge inverter, a primary compensation network, and a transmitting coil. The secondary side includes a receiving coil, a secondary compensation network, a rectifier bridge, a output filter, and

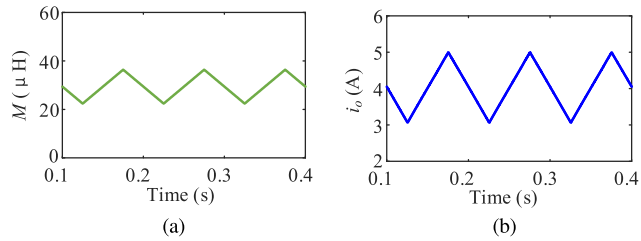

Fig. 2. Mutual inductance and load current waveform. (a) Mutual inductance. (b) Load current.

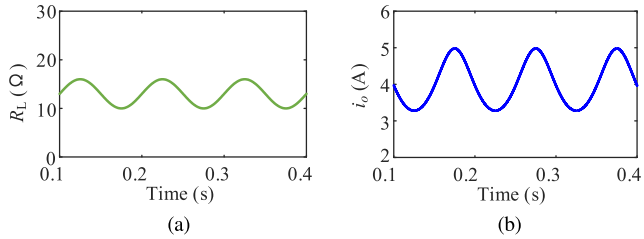

Fig. 3. Load and load current waveform. (a) Load. (b) load current.

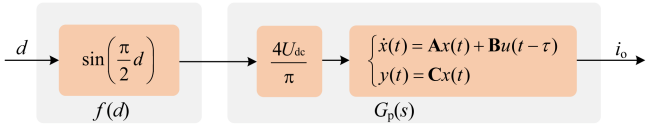

Fig. 4. Block diagram of the WPT system based on the Hammerstein model.

a load. In practical operation, the capacitance and inductance parameters mainly undergo specific changes due to environmental changes, which can cause very slow changes in the system parameters. On contrary, mutual inductance and load could fluctuate very quickly. Figs. 2 and 3 show, respectively, the load current of an open-loop simulation system under load and mutual inductance fluctuations. The system adopts the parameters shown in Section IV. It can be seen that either of the two parameters changes, the load current will also change. Therefore, feedback control is necessary to ensure the stabilize the system output.

Our previous research [28] shows that the system can be described by a Hammerstein model shown in Fig. 4, where d represents the duty cycle of PS angle (control variable), $f(d)$ is the static nonlinearity function, i_o is the load current, and $G_{\mathrm{p}}(s)$ is a linear time-invariant transfer function model. The relationship between i_{o} and d can be described as follows:

$$i_{\mathrm{o}} = G_{\mathrm{p}}(s) f(d). \tag{1}$$

The static nonlinearity corresponding to a full-bridge inverter can be readily obtained as $f(d) = \sin(\pi d/2)$. Alternatively, this nonlinear function can also be identified from static input–output data (measured after all transients have been died out). For convenient of writing, in the following text, d is replaced with the input variable u and i_o is replaced with the output variable y. The dynamic linear model can be identified from the dynamic input–output data, which are related to the transient response generated by an appropriate excitation signal, such as

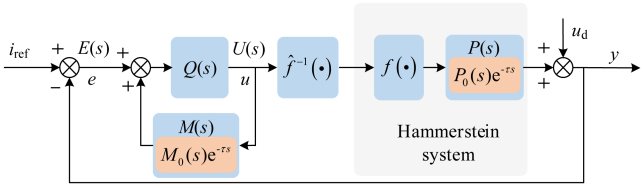

Fig. 5. Block diagram of the IMC scheme based on the Hammerstein model.

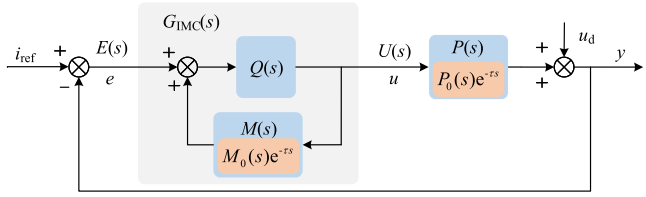

Fig. 6. Block diagram of the equivalent IMC scheme.

the pseudorandom binary sequence (PRBS). To account for the communication delay, we can add a pure delay τ to the model. Then, the Hammerstein model of the system can be written as [32]

$$\begin{cases} x_u(t) = G(s,\theta) f(u(t-\tau)) = \dfrac{B(s,\theta)}{A(s,\theta)} f(u(t-\tau)) \\ y(t_k) = x_u(t_k) + v(t_k) \end{cases} \tag{2}$$

in which $G(s,\theta)$ is a linear transfer function for the plant, $x_u(t)$ represents the time-domain response of the plant, $u(t-\tau)$ represents the delayed input, $v(t_k)$ represents the output measurement noise, $y(t_k)$ represents the output measurement, and $t_k = kT$ represents the sampling time (with T being the sampling period). $B(s,\theta)$ and $A(s,\theta)$ are the following polynomials:

$$B(s,\theta) = b_{n_\mathrm{b}} s^{n_\mathrm{b}} + b_{n_\mathrm{b}-1} s^{n_\mathrm{b}-1} + \cdots + b_0 \tag{3a}$$

$$A(s,\theta) = s^{n_\mathrm{a}} + a_1 s^{n_\mathrm{a}-1} + \cdots + a_{n_\mathrm{a}} \tag{3b}$$

where $\theta = [a_1, \ldots, a_{n_\mathrm{a}}, b_0, \ldots, b_{n_\mathrm{b}}]^\top$ is the vector of unknown parameters, with n_a and n_b ($n_\mathrm{a} \geqslant n_\mathrm{b}$) being polynomial degrees. The following optimization problem is defined to estimate the unknown model parameters:

$$\widehat{\theta}, \widehat{\tau} = \arg\min_{\theta,\tau} J(\theta,\tau) \tag{4a}$$

$$J(\theta,\tau) = \arg\min_{\theta,\tau} \frac{1}{2N} \sum_{k=1}^{N} \varepsilon^2(t_k) \tag{4b}$$

$$\varepsilon(t_k) = y(t_k) - x_u(t_k) \tag{4c}$$

where $J(\theta,\tau)$ is the cost function and $\varepsilon(t_k)$ is the output error at the kth sampling time. The Newton's steepest gradient descent method has the characteristics of fast convergence, so it is used to iteratively estimate the parameters θ and τ.

B. Hammerstein-Model-Based IMC

The Hammerstein-model-based IMC is shown in Fig. 5, where e denotes the error between the load current y and the reference i_ref, $P(s)$ and $M(s)$ denote, respectively, the WPT system and model, and $Q(s)$ denotes the internal model controller. $U(s)$ represents the output of the feedback controller, and u_d denotes the external disturbance. The control objective is to force the load current y to track the set point i_ref. When the nonlinear component $f(\cdot)$ of the system is fully compensated for, the control structure can be simplified as the one shown in Fig. 6, which is the standard IMC structure. $G_\mathrm{IMC}(s)$ denotes the feedback controller (the shadowed part of Fig. 6).

The ideal internal model controller should be $G_\mathrm{IMC}(s) = M^{-1}(s)$. However, this ideal controller is impossible to implement if $M(s)$ is not strictly proper. Therefore, a practical way is to decompose $M(s)$ as the nonminimum phase part (e.g., right-half plane zeros) $M_+(s)$ and the minimum phase part $M_-(s)$. Then, a low-pass filter $F(s) = 1/(1+\lambda s)^n$ is cascaded in the controller to ensure the stability and robustness of the closed-loop system. The practical internal model controller is designed as

$$Q(s) = F(s)/M_-(s). \tag{5}$$

The feedback controller $G_\mathrm{IMC}(s)$ can be obtained as

$$G_\mathrm{IMC}(s) = \frac{U(s)}{E(s)} = \frac{M_-^{-1}(s)}{F^{-1}(s) - M_+(s)}. \tag{6}$$

Based on our previous research, the linear part of the *LCC-S* WPT system can be described as

$$M(s) = \frac{b_0}{s^2 + a_1 s + a_2} \mathrm{e}^{-\tau s} \tag{7}$$

where b_0, a_1, a_2 represents the model parameters. $M(s)$ is decomposed as $M_+(s) = \mathrm{e}^{-\tau s}$ and $M_-(s) = b_0/(s^2 + a_1 s + a_2)$. Therefore, $G_\mathrm{IMC}(s)$ is derived as follows:

$$G_\mathrm{IMC}(s) = \frac{s^2 + a_1 s + a_2}{b_0(\lambda^2 s^2 + 2\lambda s + 1 - \mathrm{e}^{-\tau s})}. \tag{8}$$

The parameter λ is the only adjustable parameter in IMC, and it plays a role in balancing tracking speed and robustness. According to [46], considering factors, such as system robustness and disturbance rejection capability, the filter time constant λ can be chosen to be around ten times the sampling period. $M(s)$ and $P(s)$ generally do not match. According to the robustness theorem, the closed-loop stability condition of IMC is

$$|M_+(s)F(s)| \leqslant 1/l_\mathrm{m} \quad \forall\omega \tag{9}$$

where l_m is the upper bound of model uncertainties

$$E_\mathrm{m}(s) = \left| \frac{P(s) - M(s)}{P(s)} \right| \leqslant l_\mathrm{m}. \tag{10}$$

Assuming that $|M_+(s)| = 1$, when $E_\mathrm{m}(s)$ increases, $|F(s)|$ needs to be selected smaller. Since we have $M_+(0)F(0) = 1$ in IMC, the feedback error e satisfies

$$e \leqslant \frac{|1 - M_+(s)F(s)|}{1 - |M_+(s)F(s)E_\mathrm{m}(s)|} |i_\mathrm{ref} - u_\mathrm{d}| \tag{11a}$$

$$e \leqslant |1 - M_+(s)F(s))| \, |i_\mathrm{ref} - u_\mathrm{d}| = |\tilde{s}| \, |i_\mathrm{ref} - u_\mathrm{d}| . \tag{11b}$$

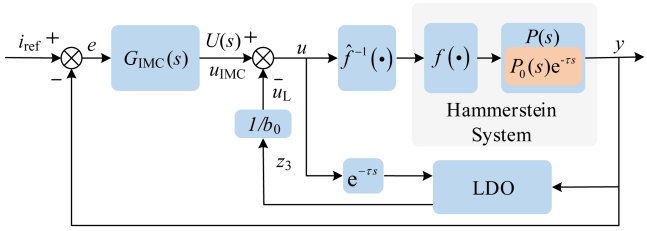

Fig. 7. Block diagram of the IMC-LDO control for the WPT system.

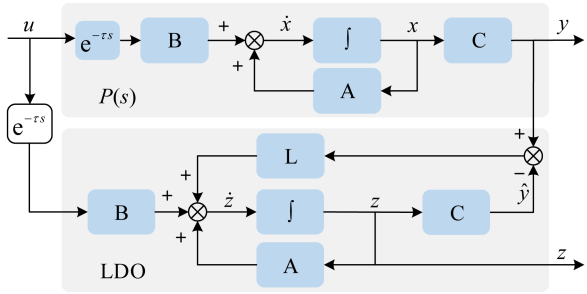

Fig. 8. Block diagram of LDO.

When control frequency $\omega \leqslant 1/\lambda$, we have $M_+(s)F(s) \approx 1$ and $e = 0$. When $\omega \geqslant 1/\lambda$, then $|F(s)|$ is very small, and $|M_+(s)F(s)E_m(s)| \approx 0$. This means that (11a) and (11b) could be identical. For both high- and low-frequency dynamics, λ should be large enough to ensure that the closed-loop response is sufficiently close to the response of the nominal $M_+(s)F(s)$. A larger λ provides greater tolerance to model uncertainty. However, in practical applications, system uncertainties are time-varying, so conventional IMC may not guarantee robustness. IMC has only one adjustable parameter, which makes tracking performance and disturbance rejection performance cannot be addressed separately. In the presence of time-varying disturbances, keeping the filter time constant of the IMC controller unchanged may not ensure system robustness. Therefore, in the following section, we shall show how the LDO can be used to address the abovementioned problem.

III. Proposed IMC-LDO Scheme

A. Control System Structure

Fig. 7 illustrates the block diagram of the IMC-LDO control structure for the WPT system. The LDO is embedded in the current control loop and is established based on the identified model. The error between the measured current and the observed current is considered as the feedback variable. The observer gains are selected through observer pole placement to ensure that the state of the system can be accurately estimated, which is the premise for disturbance estimation and compensation. The LDO can achieve the improved control performance by continuously observing the disturbance on the system output and enabling compensation in real time.

Based on the nominal model of the system described in (7), the second-order differential equation model of the system can be described as

$$\ddot{y}(t) = b_0 u(t-\tau) - a_1 \dot{y}(t) - a_2 y(t). \tag{12}$$

When parameter variations are considered, the model can be established as

$$\begin{aligned} \ddot{y}(t) = {} & (b_0 + \Delta b_0)\, u(t-\tau) - (a_1 + \Delta a_1)\, \dot{y}(t) \\ & - (a_2 + \Delta a_2)\, y(t) + u_d \end{aligned} \tag{13}$$

where Δb_0, Δa_1, and Δa_0 represent the uncertain or mismatched parts of the system parameters, and u_d represents the external disturbance such as measurement error or other factors. In this article, the total disturbance includes the parameter uncertainty and the external disturbance, and is defined as

$$\gamma(t-\tau) = \Delta b_0 u(t-\tau) - \Delta a_1 \dot{y}(t) - \Delta a_2 y(t) + u_d. \tag{14}$$

Then, (13) can be reformulated as

$$\ddot{y}(t) = b_0 u(t-\tau) - a_1 \dot{y}(t) - a_2 y(t) + \gamma(t-\tau). \tag{15}$$

Selecting state variables as

$$\begin{cases} x_1(t) = y(t) \\ x_2(t) = \dot{y}(t) \\ x_3(t) = \gamma(t) \\ h(t) = \dot{\gamma}(t). \end{cases} \tag{16}$$

The linear model can be represented in state-space form as

$$\begin{cases} \dot{x}(t) = \mathbf{A}x(t) + \mathbf{B}u(t-\tau) + \mathbf{E}h(t) \\ y(t) = \mathbf{C}x(t) \end{cases} \tag{17}$$

where

$$\mathbf{A} = \begin{bmatrix} 0 & 1 & 0 \\ a_2 & a_1 & 1 \\ 0 & 0 & 0 \end{bmatrix}, \mathbf{B} = \begin{bmatrix} 0 \\ b_0 \\ 0 \end{bmatrix}, \mathbf{E} = \begin{bmatrix} 0 \\ 0 \\ 1 \end{bmatrix}, \mathbf{C} = \begin{bmatrix} 1 \\ 0 \\ 0 \end{bmatrix}^T.$$

When the nonlinear component $f(\cdot)$ of the system is fully compensated for and the model parameters of the system are accurately estimated, the LDO structure can be simplified as the one shown in Fig. 8, which is the standard LDO structure. According to this, we have

$$\begin{cases} \dot{z}(t) = \mathbf{A}z(t) + \mathbf{B}u(t-\tau) + \mathbf{L}(y(t) - \hat{y}(t)) \\ \hat{y}(t) = \mathbf{C}z(t) \end{cases} \tag{18}$$

where

$$\mathbf{L} = \begin{bmatrix} \beta_1 & \beta_2 & \beta_3 \end{bmatrix}, \ \hat{z}(t) = \begin{bmatrix} z_1(t) & z_2(t) & z_3(t) \end{bmatrix} \tag{19}$$

are, respectively, the gain vector and the state variable of the LDO. Equation (18) can be written in a more concise form as

$$\begin{cases} \dot{z}(t) = \mathbf{P}z(t) + \mathbf{M}u(t-\tau) \\ \hat{y}(t) = \mathbf{C}z(t) \end{cases} \tag{20}$$

where

$$\mathbf{P}=\begin{bmatrix}-\beta_1 & 1 & 0\\ -\beta_2-a_2 & a_1 & 1\\ -\beta_3 & 0 & 0\end{bmatrix},\mathbf{M}=\begin{bmatrix}0 & \beta_1\\ b_0 & \beta_2\\ 0 & \beta_3\end{bmatrix},\mathbf{C}=\begin{bmatrix}1\\0\\0\end{bmatrix}^T.$$

To eliminate the disturbance $\gamma(t-\tau)$, as shown in Fig. 7, the feedforward processing is performed. The input of the WPT system $u(t)$ can be represented as

$$u(t)=u_{\mathrm{IMC}}(t)-u_{\mathrm{L}}(t) \tag{21}$$

where $u_{\mathrm{IMC}}(t)$ represents the output of the IMC controller and u_{L} represents the disturbance compensation control variable, which is computed as

$$u_{\mathrm{L}}=z_3(t)/b_0. \tag{22}$$

By combining (15), (21), with (22), we can obtain

$$\ddot{y}(t)=b_0u_{\mathrm{IMC}}(t-\tau)-a_1\dot{y}(t)-a_2y(t)+\gamma(t-\tau)-z_3(t-\tau). \tag{23}$$

When $z_3(t)$ accurately tracks the disturbance $\gamma(t)$, i.e., $z_3(t)\approx\gamma(t)$, we can obtain

$$\ddot{y}(t)=b_0u_{\mathrm{IMC}}(t-\tau)-a_1\dot{y}(t)-a_2y(t). \tag{24}$$

From (24), it can be seen that the disturbance $\gamma(t)$ is eliminated by LDO. Although the IMC controller is derived from the nominal model, the introduction of LDO will enhance the IMC system's ability to suppress disturbances.

B. Observer Parameter Design

Define the state estimation error as $\tilde{x}(t)=x(t)-z(t)$, then

$$\dot{x}(t)-\dot{z}(t)=(\mathbf{A}-\mathbf{LC})\left[x(t)-z(t)\right]+\mathbf{E}h. \tag{25}$$

The characteristic polynomial of the abovementioned equation is

$$|\rho\mathbf{I}-(\mathbf{A}-\mathbf{LC})|=\rho^3+(a_1+\beta_1)\rho^2+(\beta_1a_1+\beta_2+a_2)\rho+\beta_3 \tag{26}$$

where ρ represents the eigenvalues of $\mathbf{A}-\mathbf{LC}$. To make the estimation error $\tilde{x}(t)$ close to zero, the matrix $\mathbf{A}-\mathbf{LC}$ must be Hurwitz [47], meaning its eigenvalues have negative real parts. This can be achieved through a simple pole placement method as follows:

$$(\rho+\omega_{\mathrm{o}})^3=\rho^3+(a_1+\beta_1)\rho^2+(\beta_1a_1+\beta_2+a_2)\rho+\beta_3 \tag{27}$$

where ω_{o} represents the observer bandwidth, so the LDO parameters can be obtained as follows:

$$\begin{cases}\beta_1=3\omega_{\mathrm{o}}-a_1\\ \beta_2=3\omega_{\mathrm{o}}^2-3\omega_{\mathrm{o}}a_1-a_2+a_1^2\\ \beta_3=\omega_{\mathrm{o}}^3.\end{cases} \tag{28}$$

Generally, a rule of thumb is to set ω_{o} as 3–5 times the control bandwidth [48].

TABLE I
MAIN WPT SYSTEM PARAMETERS

Items	Symbol	Value
DC input voltage	U_{dc}	60 V
Operation frequency	f_0	100 kHz
Parallel compensation capacitance	C_{f}	102.54 nF
Primary series compensation capacitance	C_{p}	17.23 nF
Secondary series compensation capacitance	C_{s}	13.77 nF
Filter capacitance	C_{d}	470 μF
Compensation inductance	L_{f}	24.77 μH
Transmitting coil inductance	L_{p}	171.18 μH
Receiver coil inductance	L_{s}	183.22 μH
Mutual inductance	M	36.40 μH
ESR of compensation inductance	R_1	0.02 Ω
ESR of transmitting coil	R_2	0.18 Ω
ESR of receiver coil	R_3	0.19 Ω
Load	R_{L}	10 Ω

ESR: Equivalent series resistance.

Remark 1: The time delay τ in the observer's input has been introduced, so the impact of input delay on estimation accuracy can be neglected [40], [49]. The LDO in this article is designed based on the standard model. Assuming that the total disturbance is bounded, the state estimation error is also bounded, and there exists a constant $\sigma_i>0$ and a determined time $T_1>0$, such that

$$|\tilde{x}_i|\le\sigma_i,\sigma_i=O\left(1/\omega_{\mathrm{o}}^n\right),i=1,2,3\quad\forall t\ge T_1 \tag{29}$$

for a positive integer n.

Remark 2: The results presented in (29) indicate that the estimation error can be reduced to some extent. By increasing the observation bandwidth ω_{o}, the bound of the state estimation error can be arbitrarily reduced. Moreover, the establishment of LDO only requires the nominal model in (7) and the observer bandwidth ω_{o}, which makes the LDO easy to implement in real applications.

IV. SIMULATION RESULTS

In this section, simulation is performed to validate the effectiveness of the proposed method. The simulation is conducted in MATLAB/Simulink, with main WPT system parameters listed in Table I. In the simulation, either the mutual inductance or load resistance can vary respect to time, and the IMC and IMC-LDO controllers are designed to maintain the stability of the load current. The reference load current is set as $i_{\mathrm{ref}}=5$ A. The IMC parameter is set as $\lambda=8\times10^{-4}$ rad/s, while the LDO parameter is set as $\omega_{\mathrm{o}}=1.142\times10^4$ rad/s. If the mutual inductance is varying, the load remains its nominal value $R_{\mathrm{L}}=10\Omega$, while if the load is varying, the mutual inductance is set as $M=36.4\,\mu$H.

Fig. 9 compares the performance of IMC and IMC-LDO under mutual inductance disturbance. It can be shown that the peak-to-peak value of the load current is 0.4 A when IMC is applied, while this value is reduced to 0.18 A when IMC-LDO is applied. Fig. 10 compares the performance of IMC and IMC-LDO under load disturbance. It can be shown that the peak-to-peak value of the load current is 0.42 A when IMC is applied, while this value is less than 0.02 A when IMC-LDO is applied. Both examples show that the IMC-LDO method has a better disturbance rejection performance.

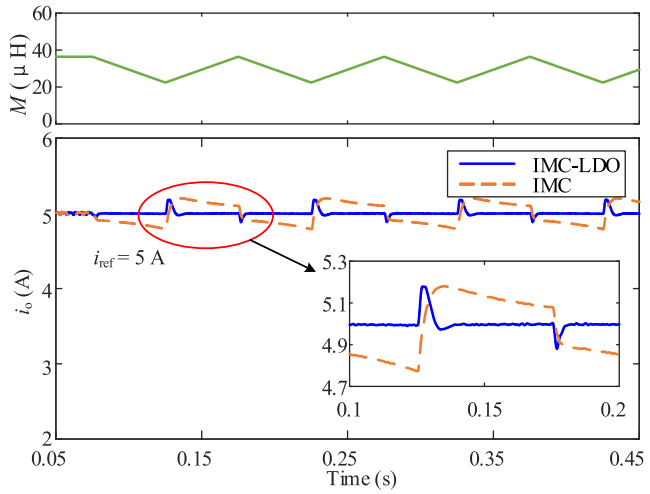

Fig. 9. Closed-loop responses of IMC and IMC-LDO under mutual inductance variations.

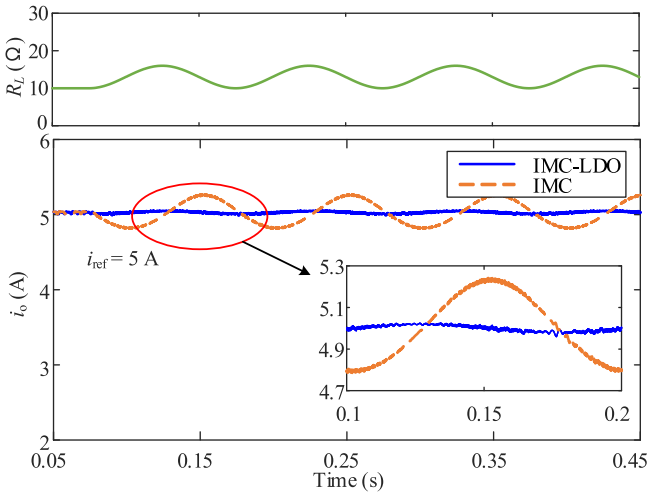

Fig. 10. Closed-loop responses of IMC and IMC-LDO under load variations.

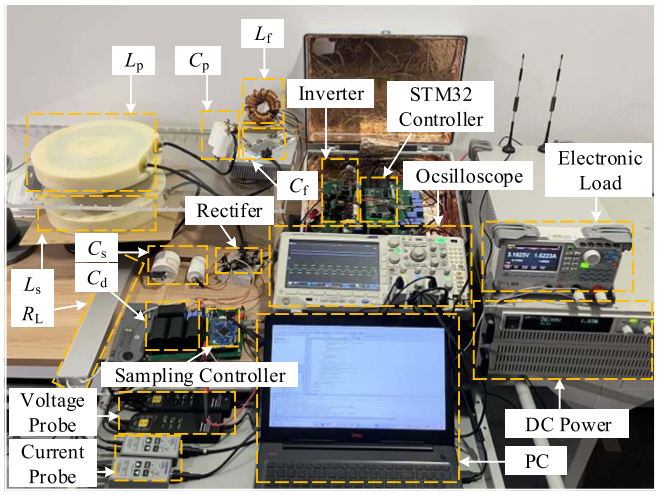

Fig. 11. Experimental setup.

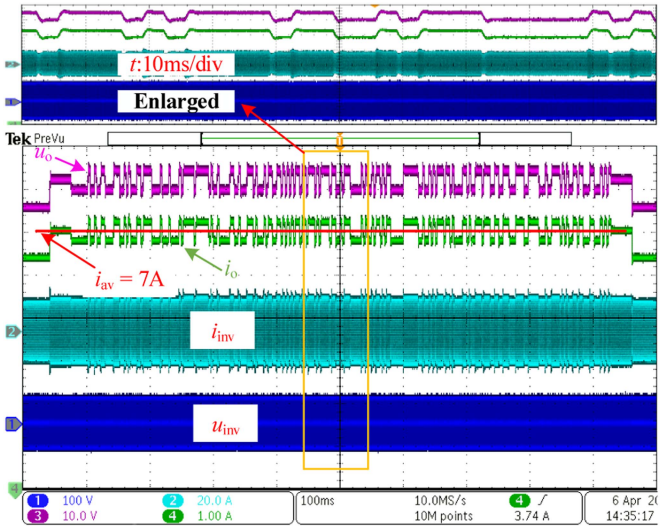

Fig. 12. Experimental data for model identification.

V. Experimental Results

In this section, experimental results are provided to verify the effectiveness of the proposed modeling and control method. The experimental setup platform is shown in Fig. 11, and the 32-b processor STM32H743 is used on the primary side to realize the IMC-LDO control, the signal processing, and the communication function. On the secondary side, the 32-b processor STM32F407 is adopted to realize the sampling and the data transmission functions. The RF device nRF2401 is adopted for wireless communication. It has the advantages of low-power consumption and high transmission rate. The data communication format is that a single batch of 5 data is combined into one packet and transmitted to the primary side. The interval for sampling each data is 60 μs. Through the data transmission testing, the communication delay is measured to be approximately 820 μs. The cement load and electronic load are connected in series to adjust the load resistance in the interval [10 17] Ω. The resistance value of the cement load is 8 Ω. The programmable electronic load RIGOL-DL3021 with the maximum power limit of 200 W is adopted to achieve load variation. The other parameters of the WPT system are shown in Table I.

A. Model Identification

Two sets of data are collected in the experiment, with each set containing 13 200 input–output data points. The sample time is 60 μs. One set of data is used for model estimation and is referred to as the identification data. Another set of data is used for cross-validation to assess the accuracy of the estimated model and is referred to as the validation data. The identification data is generated by imposing a PRBS sequence overlaid with $\pm$ 4% duty cycle on the static duty cycle $\bar{d} = 0.74$. The validation data is generated using a random number in [0 1] as the input. The load current of the system excited by the PRBS sequence is shown in Fig. 12, where CH1 and CH2 denote, respectively, the inverter output voltage u_{inv} and inverter output current i_{inv}, while CH3

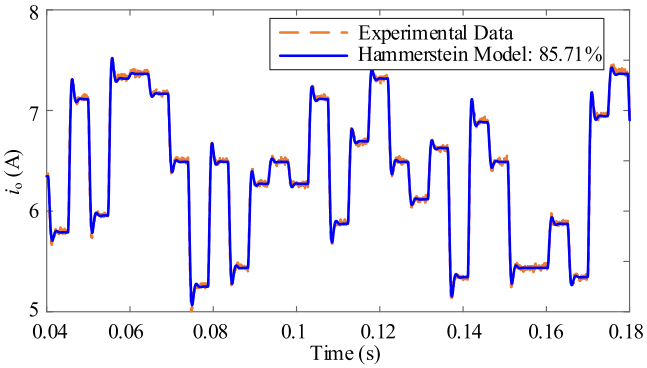

Fig. 13. Comparison of the measured output and estimated model output.

and CH4 denote, respectively, the system output voltage u_o and load current i_o. The steady-state output measurement of this working point is $i_{av} = 7$ A. Based on the identification data $\{f(d(k)), i_o(k)\}$, the linear part of the Hammerstein model $G_p(s)$ is obtained (see also [32], [33]) as follows:

$$G_p(s) = \frac{1.2431 \times 10^8}{s^2 + 3.8088 \times 10^3 s + 1.3546 \times 10^7} e^{-8.29 \times 10^{-4} s}. \tag{30}$$

The fitting ratio is used to evaluate the accuracy of the identified model. In this example, by using the MATLAB command `compare`, the fitting ratio between the estimated model and identification data excited by the PRBS sequence is computed as 82.72%. A portion of the validation data and the corresponding response of the Hammerstein model under same random input are shown in Fig. 13. The fitting ratio of the Hammerstein model is 85.71%. The high fitting ratio indicates that the Hammerstein model can effectively describe the dynamic characteristics of the system. The difference in fitting ratio between the two datasets is mainly due to different signal-to-noise ratios (SNR). The fitting ratio between the validation data and the estimated model is higher because the SNR is relatively lower when there are large variations in the random input d. Although random noise can reduce the fitting ratio between the estimated model and measured data, the obtained estimated model can still be used for system controller design. The experimental results confirm the effectiveness of the controller designed using the estimated model.

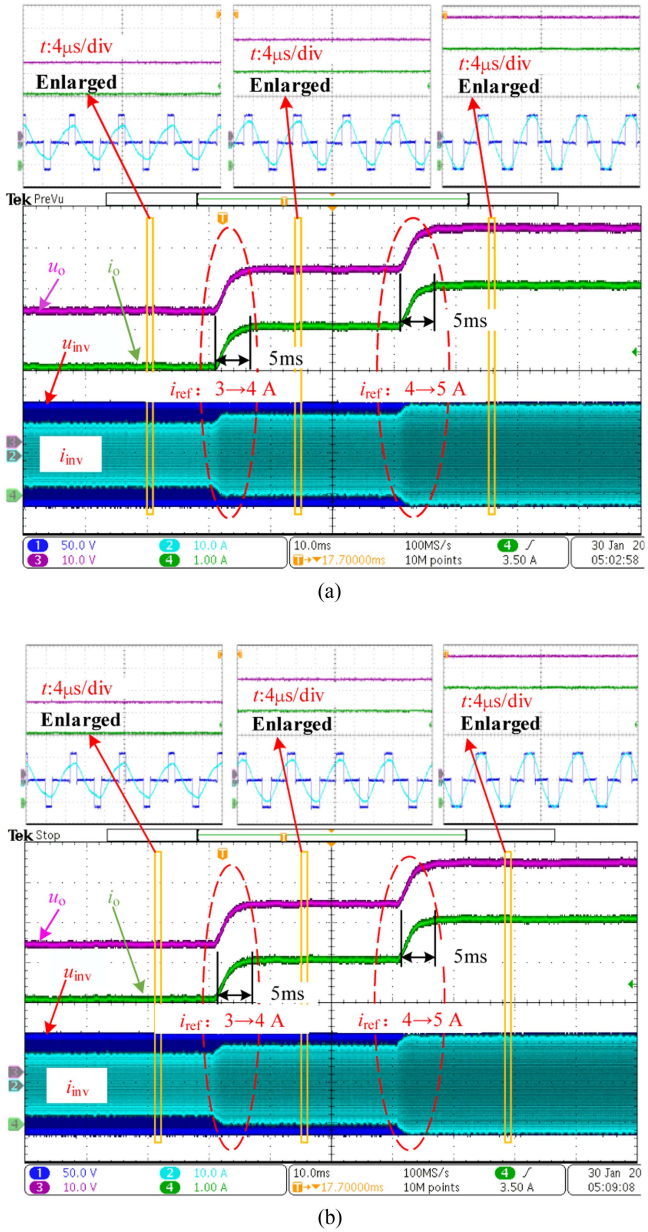

Fig. 14. Closed-loop response of different control methods under reference changes. (a) IMC-LDO. (b) IMC.

B. Validation of IMC-LDO Scheme

To verify the performance of the proposed IMC-LDO controller, set point response tests, load variation tests, and mutual inductance variation tests have been carried out. In the set point response, there are two set point changes, i.e., $i_{ref} = 3 \rightarrow 4$ A and $i_{ref} = 4 \rightarrow 5$ A. We consider two types of load variations: In the first type, the load varies in [10 17] Ω with a sinusoidal manner, while the other parameters remain the same as in Table I. In actual system operation, load variations may not be strictly sinusoidal. But typical disturbances in systems often exhibit periodic and sustained changes. Therefore, the selected sinusoidal load in this article is only used as a representative disturbance signal to evaluate the performance of the controller against sustained disturbances. In the second type of load variations, the load changes in a step manner from 13 Ω to 10 Ω. In the mutual inductance variation, the change of the mutual inductance is realized through the free-falling of the receiving coil on the secondary side by 2 cm, and this yields a mutual inductance change $M = 36.4 \rightarrow 24.4$ μH. For all tests, the control period is 60 μs.

The control performance of IMC-LDO for set point response tests and continuous disturbance tests is shown in Figs. 14(a), 15(b), and 18(b), where $\lambda = 8 \times 10^{-4}$, $\omega_o = 1.142 \times 10^4$ rad/s. As a comparison, the results of IMC control are shown in Figs. 14(c), 15(c), and 18(c), where $\lambda = 8 \times 10^{-4}$. The results of PID control are shown in Figs. 15(d) and 18(d). The static nonlinear

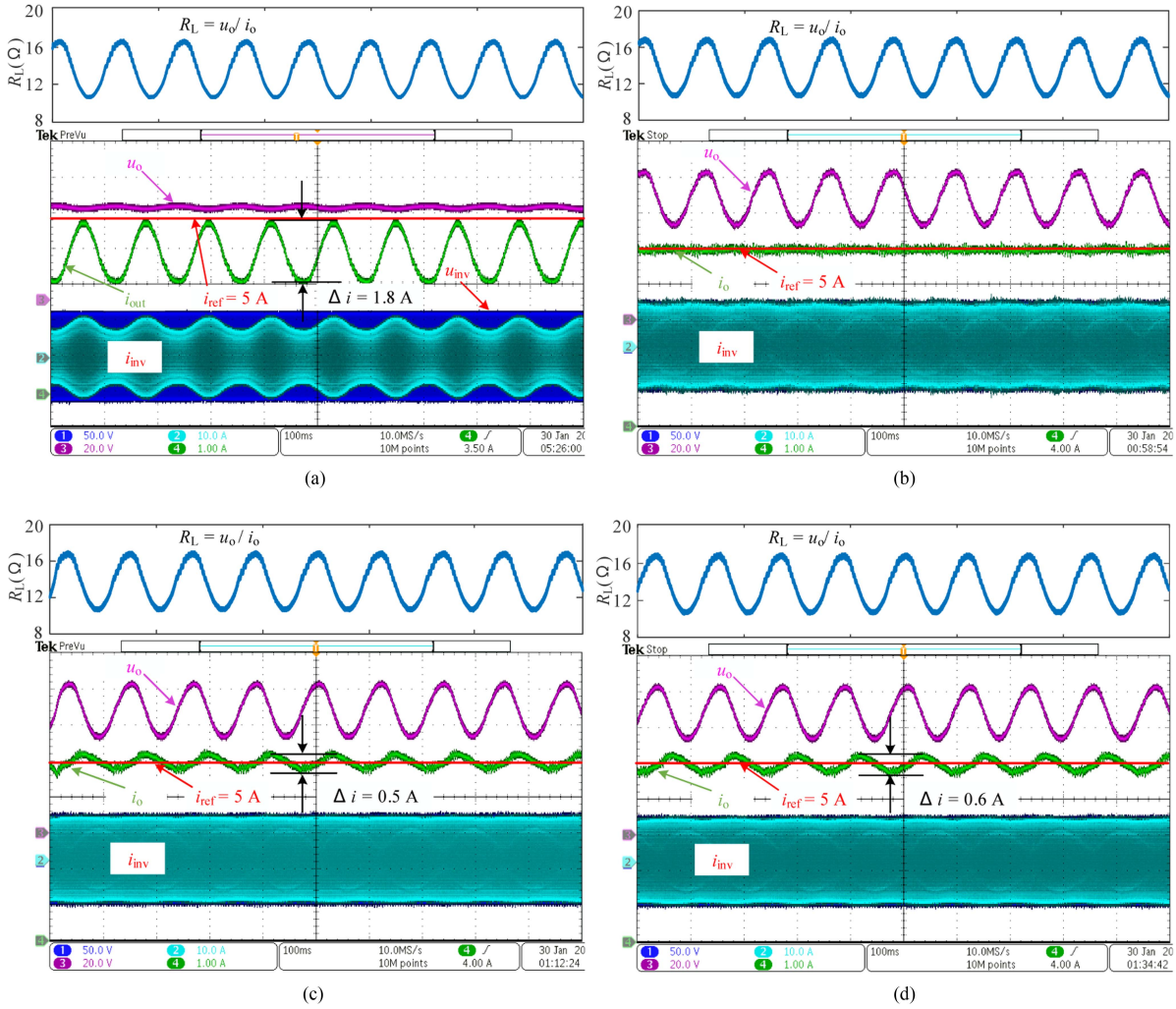

Fig. 15. System response of different control methods under continuous load variations. (a) Open loop. (b) IMC-LDO. (c) IMC. (d) PID.

gain part of the PID controller in the experiment has been optimized and compensated using look-up table methods. In the parameter design of PID, time delay is considered [28]. Figs. 15(a) and 18(a) show, respectively, the load current under load disturbance and mutual inductance disturbance, where the fixed static duty cycle is set as $\bar{d} = 0.47$. The control performance of IMC-LDO in response to abrupt load variations is presented in Fig. 16. Fig. 16(a) shows the load current of the open-loop system during the sudden load variation, where the fixed static duty cycle is set as $\bar{d} = 0.63$. Fig. 16(b)–(d) illustrates the load current waveforms of the IMC-LDO system under different gain parameters β_3, where $\lambda = 8 \times 10^{-4}, \omega_o = 1.142 \times 10^4$ rad/s.

Fig. 14 shows the transient output response with no load and mutual inductance variations. The pulse width of the inverter output voltage will increase with the increase of the load current set point. Although the communication delay exists in closed-loop control systems, both methods perform identically good, with a settling time of only 5 ms. Because the IMC-LDO and the IMC controller is designed based on the identified model, which contains enough knowledge about the system dynamics, and that the communication delay has been compensated correctly.

Fig. 15 shows the load current waveforms of different control methods under continuous load changes. The real-time resistance values are calculated by u_o/i_o. In Fig. 15(a), for a fixed duty cycle $\bar{d} = 0.47$, the fluctuation amplitude of the open-loop load current is $\Delta i = 1.8$ A. After applying closed-loop control, the maximum fluctuations in load current is reduced. The results of IMC-LDO scheme achieve the best performance [see Fig. 15(b)]. In contrast, the results of IMC are shown in Fig. 15(c), and the peak-to-peak fluctuation of the load current is $\Delta i = 0.5$ A, with a long recovery time. The results of PID scheme are shown in Fig. 15(d), and the peak-to-peak fluctuation of the load current is $\Delta i = 0.6$ A, also with a long recovery time. This indicates that the IMC-LDO scheme has the best performance in suppressing output disturbances originating from load variations.

Fig. 16 shows the load current waveforms of different control modes during the sudden load variation. In Fig. 16(a), the fluctuation amplitude of the open-loop load current is $\Delta i = 1.4$ A. In Fig. 16(b)–(d), after applying IMC-LDO control, the load current exhibits overshoot, initially increasing by approximately 1.3 A before settling back to the set value. In Fig. 16(d),

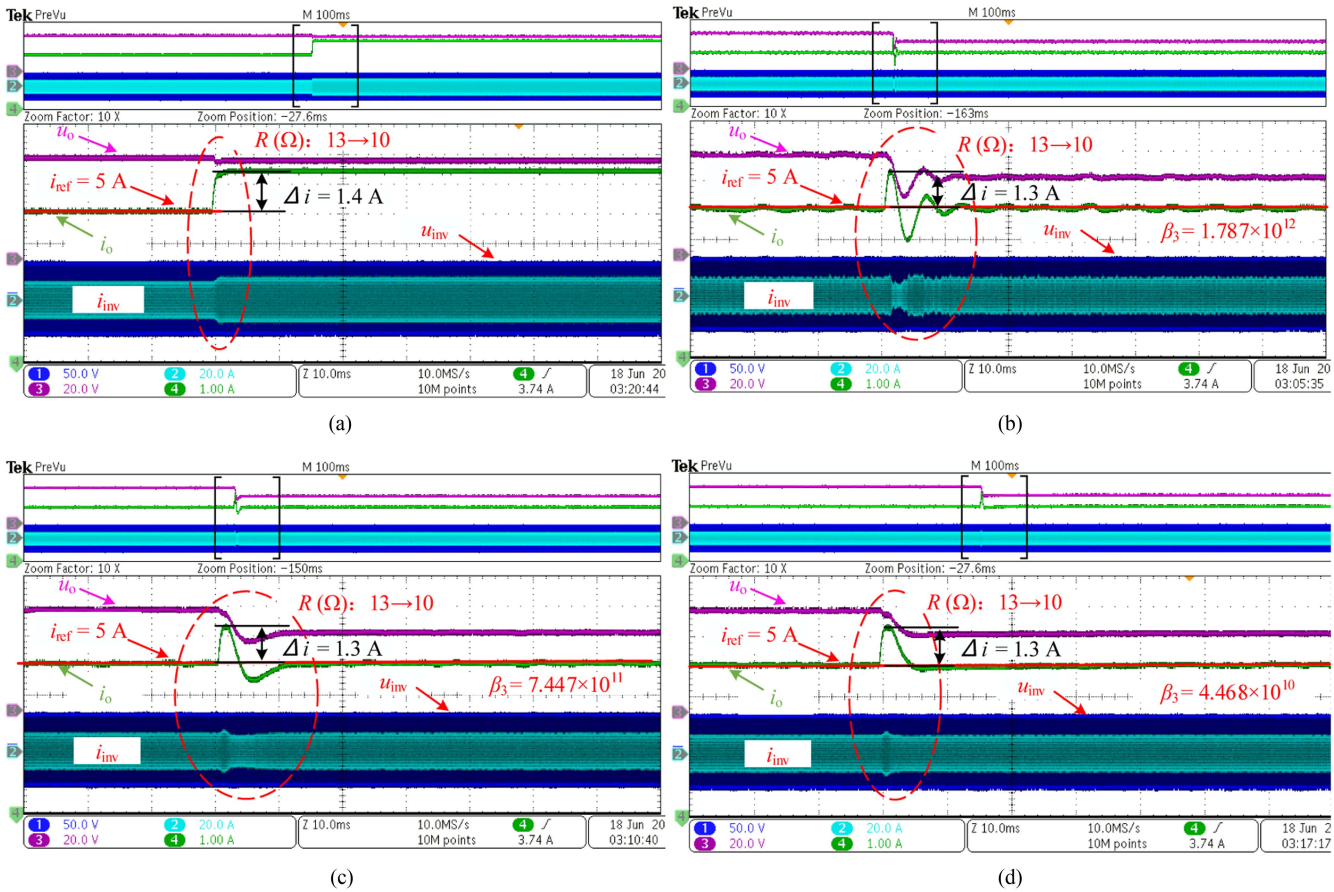

Fig. 16. System response of different control modes under the sudden load variation. (a) Open loop. (b) IMC-LDO, $\beta_3 = 1.787 \times 10^{12}$. (c) IMC-LDO, $\beta_3 = 7.447 \times 10^{11}$. (d) IMC-LDO, $\beta_3 = 4.468 \times 10^{10}$.

the scheme with $\beta_3 = 4.468 \times 10^{10}$ achieves the best performance, with no oscillations during the adjustment process and a recovery time of around 6 ms. Comparison of Fig. 16(b)–(d) demonstrates that under sudden load variations, reducing β_3 can decrease output oscillations and optimize recovery time. As a supplementary explanation, Fig. 17 shows the simulation results of the IMC-LDO system's response to sudden load changes under two different time-delay conditions. In this scenario, the load changes in a square wave pattern, switching between 13 Ω and 10 Ω. In Fig. 17, there are current disturbances with the maximum amplitude of 1.5 A and the oscillation in the output current. As the time delay decreases, both the recovery time and oscillations decrease. This indicates that reducing the delay time can also improve the control performance of the closed-loop system under sudden load variations. Based on the experimental and simulation results, it is evident that in the presence of sudden load variations, the closed-loop system output will always exhibit some unavoidable disturbances. This phenomenon is mainly caused by the following reasons: When the load changes abruptly, the quasi-constant voltage output characteristic of the *LCC-S* WPT system will lead to a corresponding sudden change in the current at the load end. Due to the response delay inherent in the WPT system, the output cannot change promptly even when the PS angle is adjusted rapidly. This will lead to output disturbances in the closed-loop

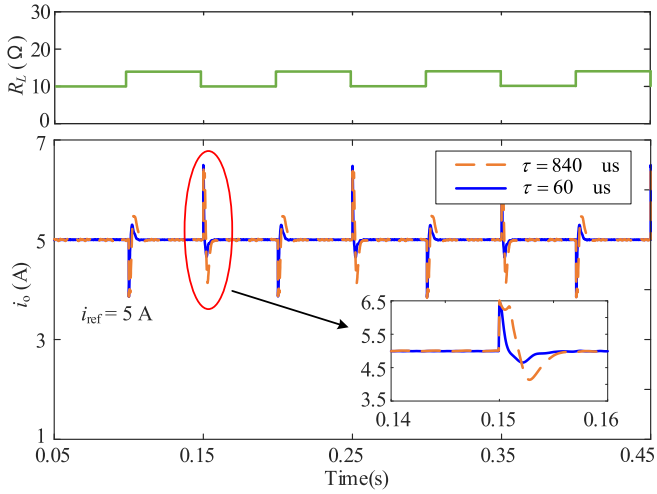

Fig. 17. Closed-loop responses of different time delay under sudden load changes.

control system during sudden load variations. By appropriately designing the parameters of the WPT system and reducing the dynamic response time of the open-loop system, the impact of the sudden disturbance can be mitigated in the closed-loop system.

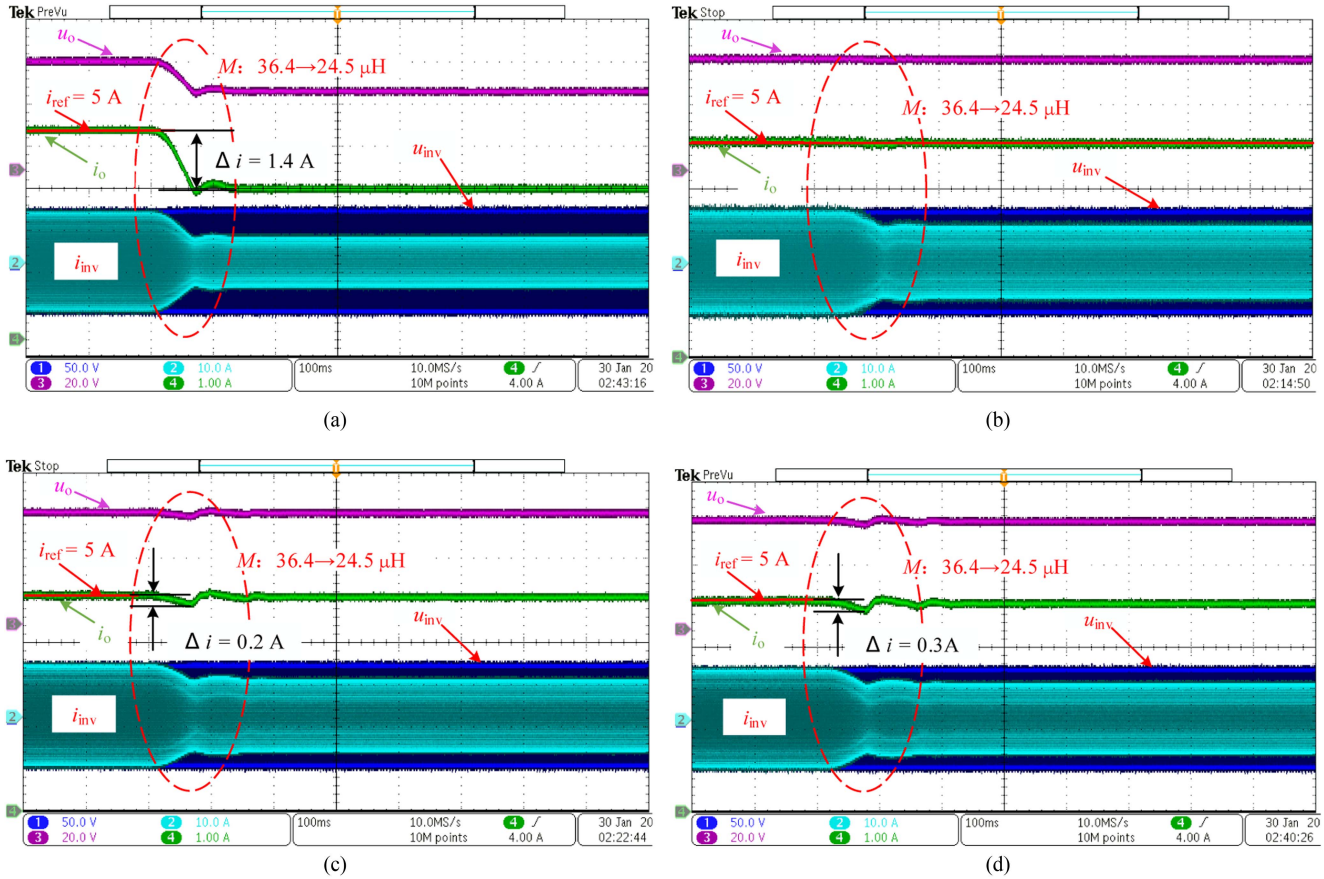

Fig. 18. System response of different control methods under mutual inductance variations. (a) Open loop (b) IMC-LDO. (c) IMC. (d) PID.

Fig. 18 shows the load current waveforms of different control methods under mutual inductance changes. In Fig. 18(a), for a fixed duty cycle $\bar{d} = 0.47$, the open-loop load current decreases and the amplitude of the change is 1.4 A. After applying closed-loop control, the amplitude of the decrease in load current is reduced and the load current has finally recovered to the set value. The results of IMC-LDO scheme achieve the best performance [see Fig. 18(b)]. In contrast, the results of IMC scheme are shown in Fig. 18(c), where the peak-to-peak fluctuation of the load current is $\Delta i = 0.2$ A, and the recovery time is about 80 ms. Under the PID scheme shown in Fig. 18(d), the peak-to-peak fluctuation of the load current is $\Delta i = 0.3$ A, and the recovery time is 80 ms. This indicates that the IMC-LDO scheme has the best performance in suppressing output disturbances under mutual inductance variations.

Moreover, the power transmission efficiency is measured through a power analyzer (HIOKI PW6001). The steady-state values of input power and output power are shown in Fig. 19. U_{dc1}, I_{dc1}, and P_{dc1} represent, respectively, input voltage, input current, and input power on the dc power supply input side. U_{dc2}, I_{dc2}, and P_{dc2} represent, respectively, output voltage, output current, and output power on the rectifier side of the WPT system. Fig. 19(a)–(c) shows the test results under different set currents I_{ref}, while Fig. 19(d) shows the experimental results under load changes when $I_{\mathrm{ref}} = 5$ A. Throughout the entire testing process, the trend of output power variation is $P_{\mathrm{out}} = 91.759 \rightarrow 163.549 \rightarrow 254.024 \rightarrow 379.310$ W and the range of power transfer efficiency η variation is $84.8\% \rightarrow 91.7\%$. As the output power of the system increases, the system efficiency also

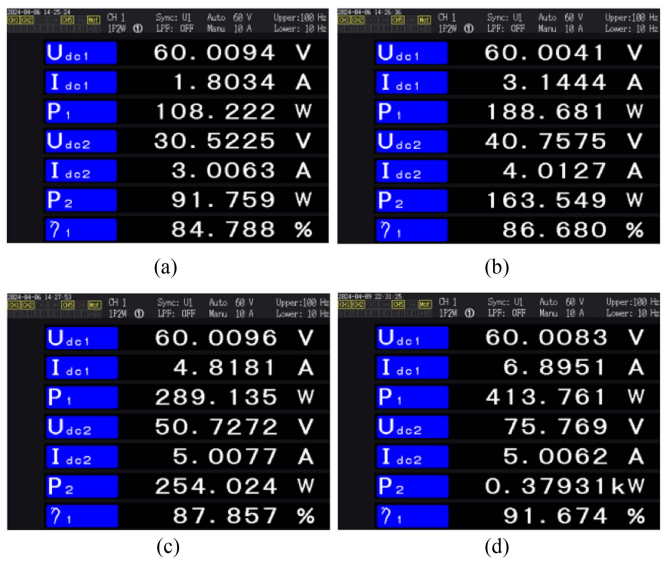

Fig. 19. Input and output of system under different set current and load. (a) $I_{\mathrm{ref}} = 3$ A and $R_{\mathrm{L}} = 10\ \Omega$. (b) $I_{\mathrm{ref}} = 4$ A and $R_{\mathrm{L}} = 10\ \Omega$. (c) $I_{\mathrm{ref}} = 5$ A and $R_{\mathrm{L}} = 10\ \Omega$. (d) $I_{\mathrm{ref}} = 5$ A and $R_{\mathrm{L}} = 15\ \Omega$.

TABLE II
COMPARISON WITH DIFFERENT CONTROL SCHEMES FOR WIRELESS CHARGING SYSTEM

References	System structures	Control algorithms	Topological complexity	Regulation time (ms)	P_{out} (W)	η (%)
[16]	Receiver buck	PIPBC	Complex	t_{Vref}: 5 t_{M}: < 1 t_{RL}: /	2630	91.1
[17]	Receiver buck-boost	DSMC	Complex	t_{Vref}: 39.3 t_{M}: / t_{RL}: /	5.5	60
[18]	Receiver buck	MPC	Complex	t_{Vref}: < 1 t_{M}: 1000 t_{RL}: /	2250	90
[20]	Receiver buck	OR-DOB	Complex	t_{Vref}: 20 t_{M}: < 1 t_{RL}: 15	121.3	76.30
[28]	Transmitter PS	PI	Simple	t_{Vref}: 24 t_{M}: / t_{RL}:19	8420	94.2
This work	Transmitter PS	IMC-LDO	Simple	t_{Iref}: 5 t_{M}: < 1 t_{RL}: < 1	379.3	91.6

increases accordingly. In this article, the stability of the closed-loop output is ensured through PS control. Experimental results mainly demonstrate the effectiveness of this control scheme under parameter disturbances. The proposed IMC-LDO scheme primarily focuses on adjusting the dynamic characteristics of the system, namely the response speed and output stability in closed-loop systems. Therefore, the implementation of soft switching and efficiency matching has not been considered during the PS control process. The nonsoft switching may result in reduced system efficiency. However, this issue can be addressed. In current research, strategies, such as dead-time compensation, passive auxiliary circuits, low-power auxiliary transformers, and auxiliary inductors, are used to extend the zero voltage switch (ZVS) range for PS control [50], [51], [52], [53], [54], thereby improving system efficiency. By designing reasonable resonance network parameters, the efficiency of the system can also be maintained at a high level.

C. System Comparison and Discussion

In Table II, some existing control methods have been compared to demonstrate the superiority of our method. The secondary-side control method, which does not require wireless communication, is primarily highlighted in the comparison. The research on indirect control methods for the primary side mainly focuses on the accuracy of parameter identification and identification time, without paying attention to the dynamic adjustment time of the system. The complex identification algorithms and unknown system parameters may lead to identification challenges. Therefore, indirect control methods for the primary side are not compared. It should be aware that we do not intend to make a fair comparison amongst these methods, because the data listed in the table are directly copied from the cited literature, rather than from a benchmark system. In Table II, t_{Vref} and t_{Iref} represent the settling time, respectively, after changing the reference set values I_{ref} and V_{ref}. t_{M} and t_{RL} represent the recovery time, respectively, under changes in mutual inductance M and load R_L. Currently, secondary-side control methods mainly involve adding additional dc–dc converters to suppress output fluctuations. In [16], when the system's output power is high, the system efficiency is close to that of the proposed method in this article. In [17], the settling time is long, and the system's output power and efficiency are relatively low. In [18], the control performance is poor under mutual inductance disturbance where recovery time is 1000 ms. When the system's output power is high, the system efficiency is close to that of the proposed method in this article. In [20], output voltage fluctuations can be effectively suppressed under conditions of varying mutual inductance. The settling time and recovery time are relatively long. The efficiency of the system is very low. In [28], the Hammerstein model was proposed to accurately describe the system's dynamic behavior based on primary-side control, which included nonlinear, linear, and time-delay link. A PI controller was designed based on this model. However, the designed controller does not account for time-varying parameter perturbations. The settling time and recovery time are relatively long.

Compared to the existing methods, our proposed IMC-LDO strategy is effective in achieving constant output current regulation and high transmission efficiency in WPT systems. Under continuous load and mutual inductance disturbances, the output current has almost no fluctuations and the settling time is short. The advantages of the method proposed in this article are summarized as follows.

1) With the primary-side PS control strategy, the need for additional dc–dc converters is eliminated, leading to increased system efficiency and reduced topological complexity of the WPT system.
2) Feedback on the output current is provided, and the time delay is thoroughly considered and compensated for, enabling accurate and fast regulation of constant output current.

3) The simplified model established includes the nonlinearity and dynamic characteristics of the wireless link. The IMC-LDO controller designed based on this model can achieve fast tracking performance and quickly ensure the stability of the output.
4) These disturbances caused by load, mutual inductance variations, noise, etc., are effectively estimated and compensated by LDO to achieve constant output regulation.

VI. Conclusion

In WPT systems, disturbances are a common phenomenon due to load and mutual inductance variations. In the application of conventional IMC in WPT systems, robustness may not be guaranteed if disturbances occur during operation. In this article, we have adopted the LDO to estimate the disturbances resulting from load and mutual inductance variations, and then designed a feedforward loop to eliminate these disturbances. This leads to the IMC-LDO control strategy that achieves simultaneously good reference tracking performance and disturbance rejection performance. In addition, we have also presented a Hammerstein-model-based identification method that is necessary for IMC-LDO parameter design, as well as a pole placement algorithm for LDO gain selection. The simulation and experimental results have verified the good disturbance rejection performance of IMC-LDO in *LCC-S* WPT system under continuous changes in load and mutual inductance parameters.

References

[1] S. Roy, A. N. M. W. Azad, S. Baidya, M. K. Alam, and F. Khan, "Powering solutions for biomedical sensors and implants inside the human body: A comprehensive review on energy harvesting units, energy storage, and wireless power transfer techniques," *IEEE Trans. Power Electron.*, vol. 37, no. 10, pp. 12237–12263, Oct. 2022.

[2] Z. Zhang, H. Pang, A. Georgiadis, and C. Cecati, "Wireless power transfer–an overview," *IEEE Trans. Ind. Electron.*, vol. 66, no. 2, pp. 1044–1058, Feb. 2019.

[3] Y. Chen et al., "A clamp circuit-based inductive power transfer system with reconfigurable rectifier tolerating extensive coupling variations," *IEEE Trans. Power Electron.*, vol. 39, no. 2, pp. 1942–1946, Feb. 2024.

[4] Z. Deng et al., "Design of a 60-kW EV dynamic wireless power transfer system with dual transmitters and dual receivers," *IEEE Trans. Emerg. Sel. Topics Power Electron.*, vol. 12, no. 1, pp. 316–327, Feb. 2024.

[5] W. Zhou, D. Tang, Z. Chen, R. Mai, and Z. He, "Non-isolation model and load virtual-grounding design method for capacitive power transfer system with asymmetric four-plate coupling interface," *IEEE Trans. Emerg. Sel. Topics Power Electron.*, vol. 12, no. 1, pp. 208–218, Feb. 2024.

[6] Z. Yan et al., "Free-rotation wireless power transfer system based on composite anti-misalignment method for AUVs," *IEEE Trans. Power Electron.*, vol. 38, no. 4, pp. 4262–4266, Apr. 2023.

[7] Y. Fan, Y. Sun, P. Deng, H. Hu, C. Jiang, and Y. Feng, "A simultaneous wireless power and high-rate data transfer system based on transient responses regulation," *IEEE Trans. Power Electron.*, vol. 38, no. 8, pp. 9362–9366, Aug. 2023.

[8] K. Song et al., "A rotation-lightweight wireless power transfer system for solar wing driving," *IEEE Trans. Power Electron.*, vol. 34, no. 9, pp. 8816–8830, Sep. 2019.

[9] C. Zhang, W. Lu, J. Zhao, X. Wu, H. Chen, and D. Xu, "A novel asymmetric magnetic coupler applied to multiple-receiver wireless charging system for automated guided vehicles," *IEEE Trans. Power Electron.*, vol. 38, no. 11, pp. 14761–14775, Nov. 2023.

[10] Y. Yao, S. Gao, J. Mai, X. Liu, X. Zhang, and D. Xu, "A novel misalignment tolerant magnetic coupler for electric vehicle wireless charging," *IEEE J. Emerg. Sel. Topics Ind. Electron.*, vol. 3, no. 2, pp. 219–229, Apr. 2022.

[11] K. Shi, C. Tang, H. Long, X. Lv, Z. Wang, and X. Li, "Power fluctuation suppression method for EV dynamic wireless charging system based on integrated magnetic coupler," *IEEE Trans. Power Electron.*, vol. 37, no. 1, pp. 1118–1131, Jan. 2022.

[12] L. Zhao, D. J. Thrimawithana, U. K. Madawala, A. P. Hu, and C. C. Mi, "A misalignment-tolerant series-hybrid wireless EV charging system with integrated magnetics," *IEEE Trans. Power Electron.*, vol. 34, no. 2, pp. 1276–1285, Feb. 2019.

[13] Z. Huang, S.-C. Wong, and C. K. Tse, "Comparison of basic inductive power transfer systems with linear control achieving optimized efficiency," *IEEE Trans. Power Electron.*, vol. 35, no. 3, pp. 3276–3286, Mar. 2020.

[14] Y. Li et al., "Analysis, design, and experimental verification of a mixed high-order compensations-based WPT system with constant current outputs for driving multistring leds," *IEEE Trans. Ind. Electron.*, vol. 67, no. 1, pp. 203–213, Jan. 2020.

[15] Y. Chen, B. Yang, Z. Kou, Z. He, G. Cao, and R. Mai, "Hybrid and reconfigurable IPT systems with high-misalignment tolerance for constant-current and constant-voltage battery charging," *IEEE Trans. Power Electron.*, vol. 33, no. 10, pp. 8259–8269, Oct. 2018.

[16] J. Liu, Z. Liu, and H. Su, "Passivity-based PI control for receiver side of dynamic wireless charging system in electric vehicles," *IEEE Trans. Ind. Electron.*, vol. 69, no. 1, pp. 783–794, Jan. 2022.

[17] Y. Yang, W. Zhong, S. Kiratipongvoot, S.-C. Tan, and S. Y. R. Hui, "Dynamic improvement of series–series compensated wireless power transfer systems using discrete sliding mode control," *IEEE Trans. Power Electron.*, vol. 33, no. 7, pp. 6351–6360, Jul. 2018.

[18] Z. Zhou, L. Zhang, Z. Liu, Q. Chen, R. Long, and H. Su, "Model predictive control for the receiving-side DC–DC converter of dynamic wireless power transfer," *IEEE Trans. Power Electron.*, vol. 35, no. 9, pp. 8985–8997, Sep. 2020.

[19] B. Zhang, S. Dong, C. Zhu, Y. Yin, and M. Zhang, "Composite control to suppress output fluctuation for receiver side of dynamic wireless power transfer system," *IEEE Trans. Power Electron.*, vol. 38, no. 5, pp. 6720–6733, May 2023.

[20] M. Zhang, Z. Liu, and H. Su, "Precise disturbance rejection for dynamic wireless charging system of electric vehicle using internal model-based regulator with disturbance observer," *IEEE Trans. Ind. Electron.*, vol. 71, no. 7, pp. 7695–7705, Jul. 2024.

[21] Z. Liu, L. Wang, Y. Guo, and S. Li, "Primary-side linear control for constant current/voltage charging of the wireless power transfer system based on the LCC-N compensation topology," *IEEE Trans. Ind. Electron.*, vol. 69, no. 9, pp. 8895–8904, Sep. 2022.

[22] Y. Guo, Y. Zhang, S. Li, C. Tao, and L. Wang, "Load parameter joint identification of wireless power transfer system based on the DC input current and phase-shift angle," *IEEE Trans. Power Electron.*, vol. 35, no. 10, pp. 10542–10553, Oct. 2020.

[23] K. Song, Z. Li, J. Jiang, and C. Zhu, "Constant current/voltage charging operation for series–series and series–parallel compensated wireless power transfer systems employing primary-side controller," *IEEE Trans. Power Electron.*, vol. 33, no. 9, pp. 8065–8080, Sep. 2018.

[24] X. Dai, X. Li, Y. Li, and A. P. Hu, "Maximum efficiency tracking for wireless power transfer systems with dynamic coupling coefficient estimation," *IEEE Trans. Power Electron.*, vol. 33, no. 6, pp. 5005–5015, Jun. 2018.

[25] C. Chen et al., "Modeling and decoupled control of inductive power transfer to implement constant current/voltage charging and ZVS operating for electric vehicles," *IEEE Access*, vol. 6, pp. 59917–59928, 2018.

[26] H. Li, J. Li, K. Wang, W. Chen, and X. Yang, "A maximum efficiency point tracking control scheme for wireless power transfer systems using magnetic resonant coupling," *IEEE Trans. Power Electron.*, vol. 30, no. 7, pp. 3998–4008, Jul. 2015.

[27] S. Zhao, C. Tang, F. Chen, D. Zhao, P. Deng, and J. Xiao, "Modeling and control of the WPT system subject to input nonlinearity and communication delay," *IEEE Trans. Power Electron.*, vol. 38, no. 11, pp. 14776–14787, Nov. 2023.

[28] Q. Deng, Z. Li, J. Liu, S. Li, P. Luo, and K. Cui, "Data-driven modeling and control considering time delays for WPT system," *IEEE Trans. Power Electron.*, vol. 37, no. 8, pp. 9923–9932, Aug. 2022.

[29] H. Li, J. Xu, F. Gao, Y. Zhang, X. Yang, and H. Tang, "Duty cycle control strategy for dual-side LCC resonant converter in wireless power transfer systems," *IEEE Trans. Transport. Electrific.*, vol. 8, no. 2, pp. 1944–1955, Jun. 2022.

[30] C.-S. Wang, G. Covic, and O. Stielau, "Investigating an LCL load resonant inverter for inductive power transfer applications," *IEEE Trans. Power Electron.*, vol. 19, no. 4, pp. 995–1002, Jul. 2004.

[31] M. Al-Greer, M. Armstrong, M. Ahmeid, and D. Giaouris, "Advances on system identification techniques for DC–DC switch mode power converter applications," *IEEE Trans. Power Electron.*, vol. 34, no. 7, pp. 6973–6990, Jul. 2019.
[32] F. Chen, A. Padilla, P. C. Young, and H. Garnier, "Data-driven modeling of wireless power transfer systems with slowly time-varying parameters," *IEEE Trans. Power Electron.*, vol. 35, no. 11, pp. 12442–12456, Nov. 2020.
[33] F. Chen, P. C. Young, H. Garnier, Q. Deng, and M. K. Kazimierczuk, "Data-driven modeling of wireless power transfer systems with multiple transmitters," *IEEE Trans. Power Electron.*, vol. 35, no. 11, pp. 11363–11379, Nov. 2020.
[34] F. Chen, H. Hu, L. Zhao, A. Padilla, and J. Hou, "A linear parameter-varying Hammerstein model for dynamic modeling of WPT systems," *IEEE Trans. Power Electron.*, vol. 38, no. 12, pp. 16230–16244, Dec. 2023.
[35] W.-H. Chen, J. Yang, L. Guo, and S. Li, "Disturbance-observer-based control and related methods—An overview," *IEEE Trans. Ind. Electron.*, vol. 63, no. 2, pp. 1083–1095, Feb. 2016.
[36] C. Xia, Y. Yan, P. Song, and T. Shi, "Voltage disturbance rejection for matrix converter-based PMSM drive system using internal model control," *IEEE Trans. Ind. Electron.*, vol. 59, no. 1, pp. 361–372, Jan. 2012.
[37] Z. Yin, C. Bai, N. Du, C. Du, and J. Liu, "Research on internal model control of induction motors based on Luenberger disturbance observer," *IEEE Trans. Power Electron.*, vol. 36, no. 7, pp. 8155–8170, Jul. 2021.
[38] K. Ohnishi, M. Shibata, and T. Murakami, "Motion control for advanced mechatronics," *IEEE/ASME Trans. Mechatronics*, vol. 1, no. 1, pp. 56–67, Mar. 1996.
[39] A. A. Godbole, J. P. Kolhe, and S. E. Talole, "Performance analysis of generalized extended state observer in tackling sinusoidal disturbances," *IEEE Trans. Control Syst. Technol.*, vol. 21, no. 6, pp. 2212–2223, Nov. 2013.
[40] P. Li, G. Zhu, and M. Zhang, "Linear active disturbance rejection control for servo motor systems with input delay via internal model control rules," *IEEE Trans. Ind. Electron.*, vol. 68, no. 2, pp. 1077–1086, Feb. 2021.
[41] K. Kósi, J. K. Tar, and T. Haidegger, "Application of Luenberger's observer in RFPT-based adaptive control—A case study," in *Proc. IEEE 14th Int. Symp. Comput. Intell. Informat.*, 2013, pp. 365–369.
[42] D. G. Luenberger, "Observing the state of a linear system," *IEEE Trans. Mil. Electron.*, vol. MIL-8, no. 2, pp. 74–80, Apr. 1964.
[43] M. H. Cervantes, A. d. C. Tellez Anguiano, J. A. Marin, E. E. Juarez, M. d. C. G. Ramirez, and J. C. Gomez, "Real-time simulation of a Luenberger observer applied to DC-DC converters," *IEEE Latin Amer. Trans.*, vol. 16, no. 3, pp. 981–986, Mar. 2018.
[44] H. Renaudineau, J.-P. Martin, B. Nahid-Mobarakeh, and S. Pierfederici, "DC–DC converters dynamic modeling with state observer-based parameter estimation," *IEEE Trans. Power Electron.*, vol. 30, no. 6, pp. 3356–3363, Jun. 2015.
[45] D. Das, S. Madichetty, B. Singh, and S. Mishra, "Luenberger observer based current estimated boost converter for PV maximum power extraction–a current sensorless approach," *IEEE J. Photovolt.*, vol. 9, no. 1, pp. 278–286, Jan. 2019.
[46] S. Endo, H. Kobayashi, C. Kempf, S. Kobayashi, M. Tomizuka, and Y. Hori, "Robust digital tracking controller design for high-speed positioning systems," *Control Eng. Pract.*, vol. 4, no. 4, pp. 527–536, 1996.
[47] Q. Zheng, L. Q. Gaol, and Z. Gao, "On stability analysis of active disturbance rejection control for nonlinear time-varying plants with unknown dynamics," in *Proc. 46th IEEE Conf. Decis. Control*, 2007, pp. 3501–3506.
[48] X. Chen, D. Li, Z. Gao, and C. Wang, "Tuning method for second-order active disturbance rejection control," in *Proc. 30th Chin. Control Conf.*, 2011, pp. 6322–6327.
[49] M. Ran, Q. Wang, C. Dong, and L. Xie, "Active disturbance rejection control for uncertain time-delay nonlinear systems," *Automatica*, vol. 112, 2020, Art. no. 108692.
[50] H. Shi, H. Wen, and Y. Hu, "Deadband effect and accurate ZVS boundaries of GAN-based dual-active-bridge converters with multiple-phase-shift control," *IEEE Trans. Power Electron.*, vol. 35, no. 9, pp. 9886–9903, Sep. 2020.
[51] Y. Jang and M. Jovanovic, "A new PWM ZVS full-bridge converter," in *Proc. 21st Annu. IEEE Appl. Power Electron. Conf. Expo.*, 2006, pp. 987–994.
[52] W. Chen, X. Ruan, and J. Ge, "A novel full-bridge converter achieving ZVS over wide load range with a passive auxiliary circuit," in *Proc. IEEE Energy Convers. Congr. Expo.*, 2010, pp. 1110–1115.
[53] Y. Jang and M. Jovanovic, "A new family of full-bridge ZVS converters," *IEEE Trans. Power Electron.*, vol. 19, no. 3, pp. 701–708, May 2004.
[54] X. Zhang, W. Chen, X. Ruan, and K. Yao, "A novel ZVS PWM phase-shifted full-bridge converter with controlled auxiliary circuit," in *Proc. 24th Annu. IEEE Appl. Power Electron. Conf. Expo.*, 2009, pp. 1067–1072.

Shijun Zhao (Member, IEEE) was born in Sichuan, China. He received the B.Eng. degree in automation from the Faculty of Information Engineering and Automation, Kunming University of Science and Technology, Yunnan, China, in 2017. He is currently working toward the Ph.D. degree in control theory and control engineering with Chongqing University, Chongqing, China.

His current research interests include modeling, system identification, and control methods of wireless power transfer and power electronics.

Fengwei Chen was born in Chongqing, China. He received the B.Eng. degree in automation and the M.Eng. degree in control theory and control engineering from Wuhan University, Wuhan, China, in 2009 and 2011, respectively, and the Ph.D. degree in automatic control from the Université de Lorraine, Nancy, France, in 2014.

From 2015 to 2016, he was a Lecturer with the Dalian University of Technology, Dalian, China. From 2017 to 2020, he was an Associate Researcher with Wuhan University, Wuhan, China. Since 2021, he has been with Chongqing University, Chongqing, China, where he is currently an Associate Professor. His research interests include system identification and parameter estimation, with applications to wireless power transfer.

Chunsen Tang (Member, IEEE) received the B.S. degree in automation and the Ph.D. degree in control theory and control engineering from the College of Automation, Chongqing University, Chongqing, China, in 2004 and 2009, respectively.

In 2008, he was a Research Fellow with the Department of Electrical and Computer Engineering, The University of Auckland, Auckland, New Zealand. In 2009, he was with the College of Automation, Chongqing University, Chongqing, China, where he is currently a Professor. His current research interests include nonlinear modeling and analysis, intelligent control, and wireless power transfer.

Pengqi Deng (Student Member, IEEE) received the B.E. degree in automation and the Ph.D. degree in control theory and control engineering from the College of Automation, Chongqing University, Chongqing, China, in 2015 and 2024, respectively.

Since 2024, he has been with the College of Optoelectronics Engineering, Chongqing University of Posts and Telecommunications, Chongqing, China, where he is currently a postdoctor. His research interests include nonlinear modeling and analysis, electromagnetic interference suppression, and wireless power transfer.

Chanzhen Duan (Student Member, IEEE) was born in Hubei, China. He received the bachelor's degree in electrical engineering and automation from the School of Electrical and Information engineering, Wuhan Institute of Technology, Wuhan, China, in 2022. He is currently working toward the master's degree in control engineering with the School of Automation, Chongqing University, Chongqing, China.

His research interests are data-based modeling and control of wireless power transmission systems.